PNAS RESEARCH ARTICLE | BIOPHYSICS AND COMPUTATIONAL BIOLOGY

Ultraslow conformational dynamics and catch bond formation of a bacterial adhesin revealed by a single-domain variant of FimH

Pearl Magala[a,1], Lisa M. Tuttle[a,1], Gianluca Interlandi[b], Laura A. Carlucci[b,2], Molly Y. Mollica[b,3], Maria K. Janowska[a], Wendy E. Thomas[b,4], Evgeni V. Sokurenko[c,4], and Rachel E. Klevit[a,4]

Affiliations are included on p. 10.

Edited by Ralph R. Isberg, Tufts University School of Medicine, Boston, MA; received July 17, 2025; accepted April 30, 2026

Bacterial fimbrial adhesins such as FimH are critical for host colonization and persistence under the mechanical forces encountered at sites of infection such as the urinary tract. The molecular mechanisms by which FimH, a key virulence factor of uropathogenic *Escherichia coli*, regulates its binding to host cell surface mannose moieties through conformational switching remain incompletely understood. FimH operates across a range of conformations that includes low- (LAS), intermediate-, and high-affinity (HAS) states and forms catch bonds that paradoxically strengthen under force. The allosteric pathways governing these transitions remain poorly defined due to experimental limitations that restrict understanding of key dynamic phenomena that underlie ligand-triggered conformational shifts and force-induced long-lived interactions. Such understanding is central to drug discovery efforts to target bacterial adhesion. Here, we present a model system that fully recapitulates the conformational repertoire of FimH in the absence of its pilin domain. Our findings demonstrate that a single mutation in the lectin domain stabilizes the LAS while allowing for ligand-binding-induced transition to a HAS-like conformation and catch bond formation, mirroring the behavior of the native FimH adhesin. We propose a dynamic allosteric mechanism that involves ultraslow, low-frequency dynamics for the ability of FimH to sustain long-lived interactions with mannose, under both static and force conditions.

adhesins | catch bond | protein dynamics | lectin domain | bacterial pathogens

Significance

Urinary tract infections (UTIs) are among the most common bacterial infections. Their initiation depends on the ability of uropathogenic *Escherichia coli* (UPEC) to adhere to bladder cells. Adhesion is mediated by FimH, a two-domain protein on the UPEC surface that binds mannose-containing glycoprotein receptors and strengthens its grip under shear stress via a catch bond mechanism. To investigate FimH function, we engineered a single-domain variant that can adopt both low- and high-affinity states of FimH and can form catch bonds. We found that FimH is governed by ultraslow conformational dynamics that vary among structurally similar states. These findings provide a mechanistic framework for developing antiadhesive therapies that target FimH dynamics, offering an alternative strategy to prevent and treat UTIs.

The urinary tract, a hostile environment of constant fluid flow, poses a challenge for bacterial adhesion and colonization. Yet *Escherichia coli*, the leading cause of urinary tract infections (UTIs) (1, 2), thrives in this dynamic setting, due largely to the conformational capabilities of its molecular adhesin, FimH (3, 4). Located at the tip of type 1 fimbriae, FimH acts as a molecular pincer that can grip or release mannose moieties present on the surface of host cells. Importantly, FimH exhibits catch bond behavior, in which binding is longer-lived under shear forces such as urine flow, than under static conditions. FimH's ability to form catch bonds is essential for bacterial survival and virulence (5–10). However, the mechanisms underlying the conformational dynamics and allosteric regulation of FimH remain poorly understood at the molecular and atomistic level.

Substantial structural information on FimH has revealed three conformational states for the two-domain protein (Fig. 1*A*). Architecturally, a lectin domain (LD) that binds mannose sits atop a pilin domain (PD) that connects FimH to a fimbria. The mannose-binding loops are on the opposite end of the domain from the PD-contacting surface (Fig. 1) (11–14). Structures of LDs in the low affinity (or "inactive") state (LAS) and the high affinity (or "active") state (HAS) are shown in Fig. 1*B* (5, 15). Overall, the β-sheet structure that defines the domain is conserved in the two states, but numerous other structural elements differ (shown in color in Fig. 1*B*). For example, the Clamp loop opens away from the two mannose-binding loops, producing a widened mannose-binding pocket in the LAS but is closed along with the mannose-binding loops creating a narrower pocket in HAS. At the other end of the LD, the Insertion and Linker loops are close to the protein core in the LAS but extend outward in the HAS, contributing to its elongated structure. Collectively, these changes result in a LAS structure that is ~11 Å shorter than the HAS (16). A structure that contains both bound mannose and LD–PD interactions, referred to as IAS, is proposed to represent a transient intermediate populated during the transition from LAS to HAS (5).

Substantial evidence supports a model in which the PD allosterically regulates mannose binding by stabilizing the LAS. Domain separation allows the conformational change in

The authors declare no competing interest.

This article is a PNAS Direct Submission.

[1]P.M., and L.M.T. contributed equally to this work.

[2]Present address: Bonum Therapeutics, Seattle, WA 98109.

[3]Present address: Department of Mechanical Engineering, University of Maryland, Baltimore County, MD 21250.

[4]To whom correspondence may be addressed. Email: wendyt@uw.edu, evs@uw.edu, or klevit@uw.edu.

This article contains supporting information online at https://www.pnas.org/lookup/suppl/doi:10.1073/pnas.2519139123/-/DCSupplemental.

Published May 27, 2026.

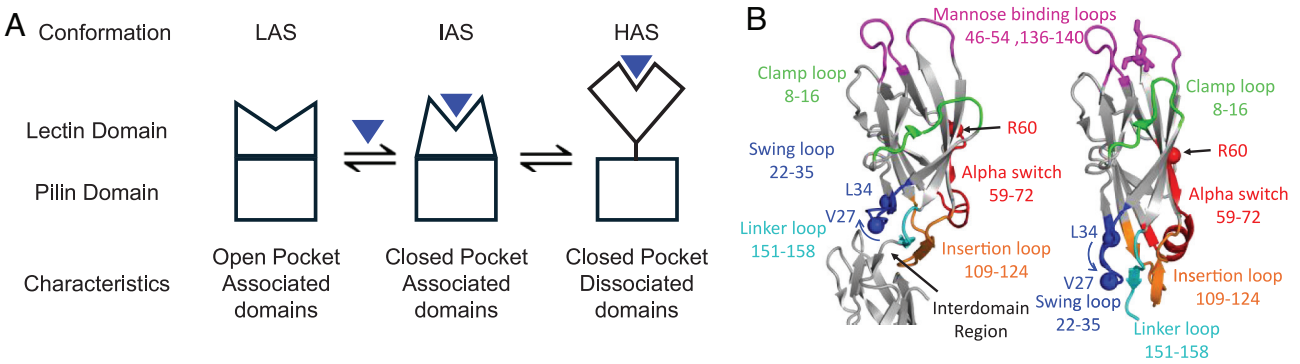

Fig. 1. FimH conformational states. (*A*) FimH adopts LAS, IAS, and HAS conformations, characterized by "open pocket and associated domains (LAS)," "closed pocket and associated domains (IAS)," and "closed pocket and dissociated domains (HAS)." (*B*) Cartoon representation of $FimH^{FL}$ showing the LAS (*Left*; PDB: 4XO9) and HAS (*Right*; PDB:1UWF). The colored regions differ substantially between the LAS and HAS. The sites of mutagenesis (spheres) allow LD to adopt LAS.

the LD associated with high-affinity binding (HAS) (Fig. 1*A*) (5). Domain separation brought about by shear force enables the long-lived binding of FimH-containing fimbriae to ligands (i.e., formation of catch bonds). Consistent with contacts between the LD and PD stabilizing the LAS conformation, isolated LDs (i.e., truncated before the PD) spontaneously adopt the HAS even in the absence of mannose (17, 18). This behavior indicates that the LD's HAS is intrinsically the lower free-energy conformation and that interdomain contacts inhibit its adoption. Efforts to stabilize the LAS in the absence of the PD have met with partial success. Substitution in the Alpha-switch region, R60P, or introduction of a disulfide bond within the Swing loop, V27C-L34C (hereafter referred to as S–S), both produce LAS in the absence of the PD, confirming that the LAS can be stabilized by forces other than contact with the PD (17, 19, 20). However, neither of these variants can convert to the HAS upon interaction with mannose.

To design a version of the LD that both spontaneously adopts the LAS and retains its ability to transition to the HAS, we considered LD residues dubbed "toggle switches" that undergo large changes in their side-chain solvent accessibility between LAS and HAS conformations (21). We found that substitution of aliphatic Leu34, whose side chain is solvent-exposed in LAS and core-buried in HAS, with charged lysine creates a protein with the desired properties: the LD carrying L34K ("$L34K^{LD}$") adopts LAS in the absence of the PD and mannose and transitions to HAS upon mannose binding (*SI Appendix*, Fig. S6*B*). Thus, $L34K^{LD}$ is a single-domain LD variant capable of recapitulating the behavior that underlies the function of full-length FimH ($FimH^{FL}$). The ability to create a single-domain allosteric model enabled the use of biochemical and biophysical approaches that are not possible with the full-length protein. We used a combination of biochemical binding experiments, NMR spectroscopy, hydrogen–deuterium exchange (HDX), atomic force microscopy (AFM), and molecular dynamics (MD) simulations to investigate the functional, conformational, and dynamic properties of $L34K^{LD}$. The results confirm that the single domain $L34K^{LD}$ displays mannose-binding kinetics similar to the full-length protein and adopts the LAS and HAS conformations in the absence and presence of mannose, respectively. Finally, we demonstrate that fimbria-incorporated FimH-L34K forms a long-lived bond with mannose under force and enables bacteria to aggregate red blood cells (RBCs) under shear conditions—a property that reflects catch bond formation. Altogether, the results elucidate an allosteric network that enables communication between the mannose-binding pocket at one end of the LD and the interdomain region at the other and, ultimately, the allosteric transition that gives rise to the enigmatic catch bond behavior.

Results

NMR Similarity Analysis Allows Conformational Classification of LD Variants. Structures of WT^{LD} with and without ligand and of $R60P^{LD}$ in the absence of ligand have been previously determined (15, 19, 22, 23). WT^{LD} adopts HAS in both cases and the structure of $R60P^{LD}$ is identical to the LAS structure of the LD as observed in $FimH^{FL}$ (C_α RMSD below 0.5 Å) (24). The (^{1}H, ^{15}N)-HSQC NMR spectrum of a protein reflects its conformation, i.e., spectra of the same protein in two different conformations will differ. We used NMR spectroscopy to ascertain conformations adopted by position 34 variants using spectra of WT^{LD} and $R60P^{LD}$ as reference states for HAS and LAS, respectively.

(^{1}H, ^{15}N)-HSQC NMR spectra were collected for each variant in the absence and presence of excess methyl α-D-mannopyranoside (referred to as mannose). Visual inspection revealed striking similarities among certain spectra and large differences in others. For example, the spectra of WT^{LD} and $L34A^{LD}$ in the absence of mannose are almost identical (*SI Appendix*, Fig. S1) while the spectra of WT^{LD} and $R60P^{LD}$ are markedly different and spectra of $R60P^{LD}$ and $L34K^{LD}$ are highly similar (Fig. 2 *A* and *B*). These qualitative comparisons suggest that $L34A^{LD}$ is in the HAS (like WT^{LD}) in the absence of ligand and $L34K^{LD}$ is in LAS (like $R60P^{LD}$).

To build on the qualitative observations, we developed a chemical shift distance (CSD) metric between two HSQC spectra (*SI Appendix*, Fig. S2 *B* and *C*). Briefly, peaks in two spectra are paired so that the summed total distance between peaks is minimized. The similarity score corresponds to the average CSD for all peaks. Low CSD values indicate high spectral similarity. CSD scores for all spectral pairs are shown as a heat-map matrix (Fig. 2*C* and *SI Appendix*, Fig. S2*A*). Consistent with visual inspection, WT^{LD} shows high dissimilarity to $R60P^{LD}$ and to $L34K^{LD}$ in the absence of mannose, indicating that the mutants adopt conformations different from WT^{LD}.

Because the CSD approach does not require peak assignments, we validated it by independently assigning all spectra except for mannose-bound $R60P^{LD}$, using conventional (^{13}C, ^{15}N) 3D NMR experiments (25) and calculating the average chemical shift perturbation (CSP) for each pair of spectra. The CSP scores (Fig. 2*C*, upper triangle) are numerically higher than the CSD scores but show identical patterns and rankings. These results confirm that CSD accurately captures conformational similarity while avoiding the need for full spectral assignment, saving substantial time, effort, and resources.

With few exceptions, spectra of LD variants fall into two categories: 1) high similarity to WT^{LD} and low similarity to $R60P^{LD}$ or 2) low similarity to WT^{LD} and high similarity to $R60P^{LD}$. Based on the known conformational states of WT^{LD} and $R60P^{LD}$, the states of all other variants were assigned as summarized in Fig. 2*D*.

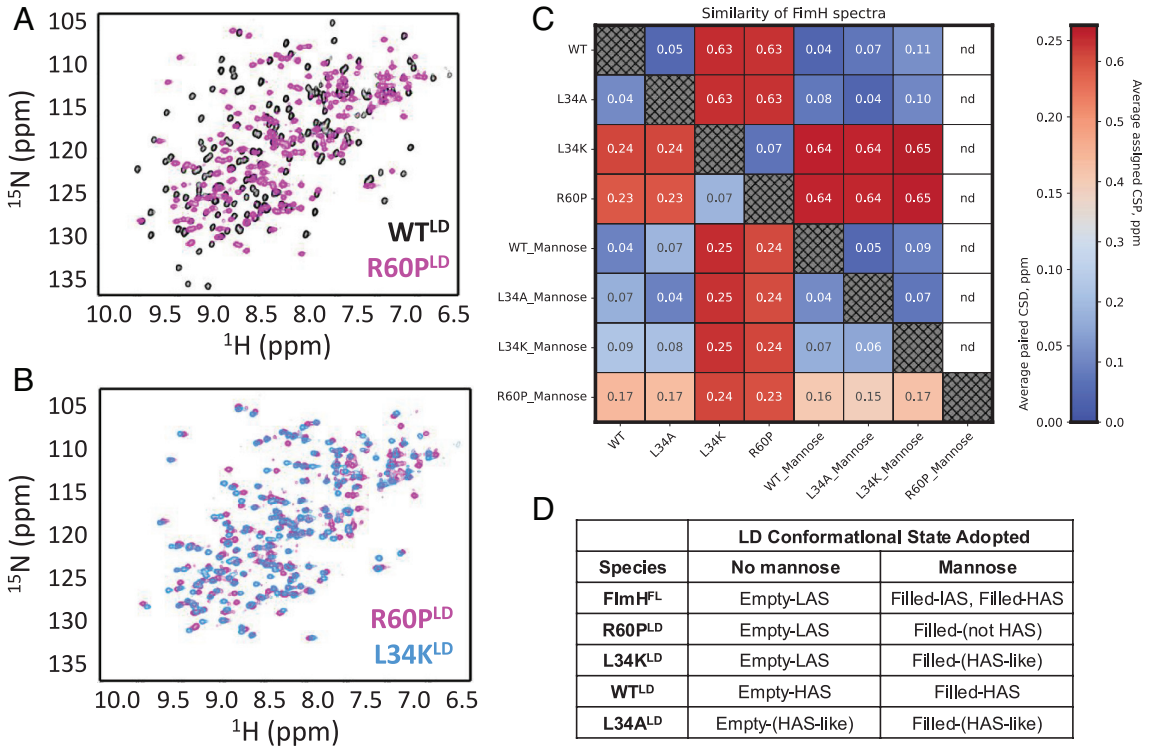

	LD Conformational State Adopted	
Species	**No mannose**	**Mannose**
FimH^{FL}	Empty-LAS	Filled-IAS, Filled-HAS
R60P^{LD}	Empty-LAS	Filled-(not HAS)
L34K^{LD}	Empty-LAS	Filled-(HAS-like)
WT^{LD}	Empty-HAS	Filled-HAS
L34A^{LD}	Empty-(HAS-like)	Filled-(HAS-like)

Fig. 2. NMR analysis of LD conformational states. (*A*) Overlay of (^{1}H,^{15}N)-HSQC spectra of WT^{LD} (black) and R60P^{LD} (magenta) indicate distinct conformations. (*B*) Overlay of R60P^{LD} (magenta) and L34K^{LD} (blue) shows highly similar spectra, indicating the same conformation. (*C*) Pairwise spectral similarity quantified by Chemical Shift Distance (CSD; *Lower Left*) or assigned chemical shift perturbation (CSP; *Upper Right*; nd, not determined) for LD variants ± mannose. (*D*) Conformational states assigned from CSD analysis.

WT^{LD} and L34A^{LD} adopt empty and filled HAS that differ only near the mannose-binding pocket. As previously reported, isolated WT^{LD} adopts a high-affinity conformation and shows only limited spectral changes when ligand is present (*SI Appendix*, Fig. S3) (16, 22, 24, 26). L34A^{LD} behaves identically. In both proteins, residues exhibiting significant CSP (CSP > 0.05 ppm) localize to the mannose-binding pocket, i.e., the two binding loops and the Clamp loop (*SI Appendix*, Fig. S3), indicating that ligand binding produces only local changes. Thus, the spectra of WT^{LD} and L34A^{LD} capture two conformations—"empty-HAS" and "filled-HAS"—that differ only within the ligand-binding pocket. This behavior contrasts with that of the LD in FimH^{FL}, which undergoes large ligand-dependent conformational changes among LAS, IAS, and HAS.

R60P^{LD} adopts LAS but fails to achieve HAS. A crystal structure of isolated R60P^{LD} is identical to WT^{LD} in the PD-bound state, demonstrating that R60P^{LD} adopts the LAS conformation (19). Consistent with prior NMR analysis (19), R60P^{LD} shows a large ligand-induced spectral change (CSD = 0.23 ppm) upon mannose binding. However, comparison of mannose-bound R60P^{LD} with WT^{LD} yields an intermediate CSD score (0.16 ppm; range 0.04 to 0.25 ppm for all scores measured), indicating that R60P^{LD} does not fully adopt a HAS-like conformation (Fig. 2*C*). At the residue level, CSPs localize to two regions: a patch surrounding R60 and a ring of residues in the interdomain region (*SI Appendix*, Fig. S4). Together, these data indicate that although the mannose-binding loops adopt a WT-like conformation, ligand-induced conformational changes are not effectively transmitted to the distal region of the LD, in contrast to the WT domain.

L34K^{LD} adopts both the LAS and HAS conformations. In the absence of ligand, the NMR spectrum of L34K^{LD} closely matches that of LAS-forming R60P^{LD} (CSD = 0.07 ppm), indicating spontaneous adoption of the LAS conformation. Upon mannose binding, L34K^{LD} undergoes extensive chemical shift changes and its spectrum becomes nearly identical to that of WT^{LD} (CSD = 0.07 ppm), demonstrating conversion to a conformation that resembles filled-HAS, which we call HAS-like. The few residue-level chemical shift differences observed localize to positions adjacent to the mutation site, indicating that they arise from the amino acid substitution rather than from a distinct conformation (*SI Appendix*, Fig. S5). In contrast, substitution of L34 with alanine fails to stabilize LAS (see above), indicating that side-chain size, polarity, and/or charge contribute to toggle function.

In sum, comparison of the NMR spectra of four LD variants distinguishes four conformational states: empty-LAS, empty-HAS, filled-HAS, and a state that is filled but not equivalent to HAS, which we call "filled-(not HAS)." The conformations adopted by each variant in the absence and presence of mannose are summarized in Fig. 2*D*. Notably, L34K^{LD} fully recapitulates the conformations observed in FimH^{FL}, adopting LAS in the absence of mannose and transitioning to a HAS-like conformation upon mannose binding.

Substitution of Toggle Switch L34 in Fimbriae Inhibits Transition to the HAS Conformation. To assess LD conformational states in the fimbrial context, we used a monoclonal antibody that specifically recognizes the HAS conformation of FimH called mAb21 (27–29). Binding of mAb21 to fimbria was measured by ELISA as a function of mannose concentration (Fig. 3 *A* and *B*). WT FimH and the L34A variant showed little to no binding in the absence of mannose and increased binding with increased mannose concentration, consistent with adoption of HAS upon ligand binding. In contrast, fimbrial variants containing charged substitutions at L34 (L34E and L34K) exhibited low (L34E^{LD}) or no (L34K^{LD}) mAb21 binding even at the highest mannose concentration, indicating a failure to adopt the HAS conformation recognized by mAb21 under assay conditions. This effect does not

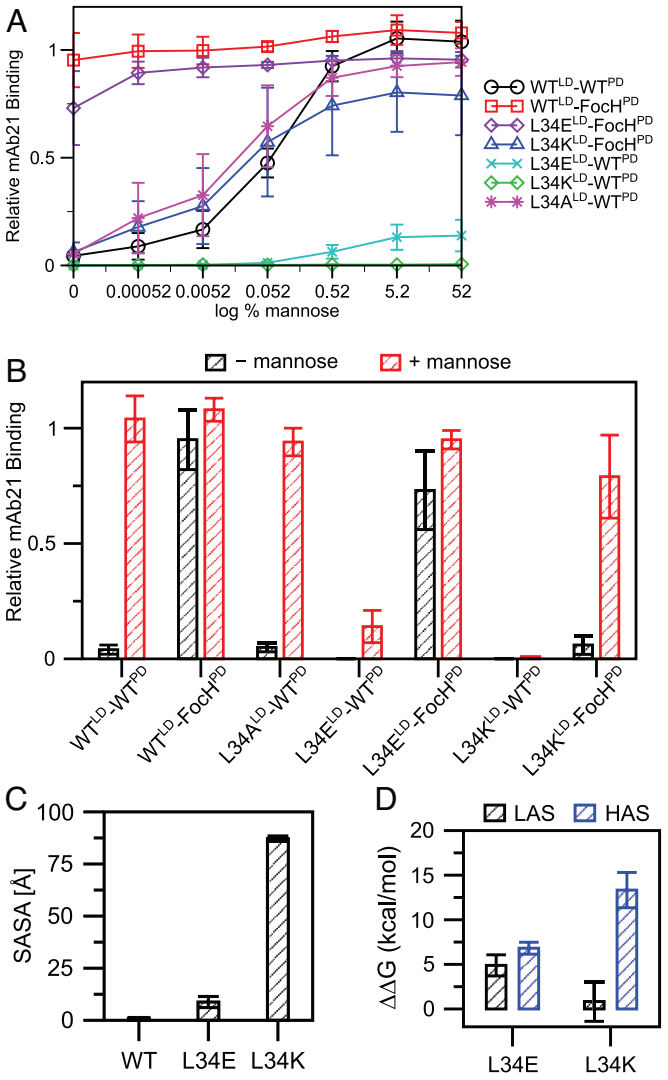

Fig. 3. Identity of toggle-switch residue determines HAS/LAS preference and transition. (*A*) Binding of HAS-specific monoclonal antibody, mAb21 as a function of increasing mannose concentration. The ability to adopt HAS was measured by ELISA for constructs containing WT^{LD}, and three substitutions at Leu34. (*B*) Observed levels of mAb21 binding relative to WT FimH binding at 2% mannose [data from (*A*)]. Black bars, binding in the absence of mannose; red bars, binding in the presence of 2% mannose. (*C*) Solvent accessibility of residue 34, averaged over the last 40 ns of a 50 ns MD simulation of the HAS LD. (*D*) Free energy calculations indicate that the L34K substitution induces greater destabilization of the HAS conformation compared to L34E. Error bars show the SEM of two simulations (n = 3).

arise from direct disruption of the mAb21 epitope, as L34 lies outside the mapped epitope (30, 31).

Because isolated $L34K^{LD}$ adopts HAS according to NMR, its inability to do so in the fimbrial context implies that the L34K mutation disrupts allosteric coupling between mannose binding and PD disengagement. To test this, we examined variants in the context of FimH-FocH hybrid PD ($FocH^{PD}$) that is incompatible with the LD and does not inhibit HAS formation (*SI Appendix*, Fig. S6*A*) (6, 18, 32). In the $FocH^{PD}$ background, WT^{LD} is fully bound by mAb21 even in the absence of mannose, confirming that loss of PD–LD contact is sufficient to drive transition to HAS. $L34E^{LD}$ behaves similarly. In contrast, the $L34K^{LD}$ chimera exhibits mannose-dependent mAb21 binding behavior, indicating that it adopts LAS without mannose and transitions to HAS only upon mannose binding (Fig. 3 *A* and *B*). Notably, its mannose concentration dependence closely resembles that of WT-FimH, implying that mannose affinity is preserved. Together, these results demonstrate that although $L34K^{LD}$ can bind mannose and adopt HAS, it inhibits the LAS-to-HAS transition in full-length FimH, even in the presence of high mannose.

Lysine at Residue 34 Disfavors Empty-HAS. We substituted the toggle-switch residue Leu34 with Lys and Glu because this side chain is buried in HAS and solvent-exposed in LAS (*SI Appendix*, Fig. S6*B*). Unexpectedly, mAb21 binding showed that the two charged residues are accommodated differently. To explore this, we performed MD simulations of $L34K^{LD}$ and $L34E^{LD}$ and compared them to published WT^{LD} simulations (33). Simulations were initiated from the HAS conformation with the side chains at position 34 oriented toward the protein core. Solvent-accessible surface area (SASA) values converged within the first few nanoseconds (*SI Appendix*, Fig. S6*D*). SASA values averaged over the final 40 ns of 50-ns trajectories (Fig. 3*C*) show the WT Leu34 side chain remained almost completely buried (<1% solvent exposure) (34) and Glu34 showed only a modest, statistically insignificant increase in exposure (~5%; $P > 0.1$). In contrast, Lys34 became substantially solvent exposed (41%; $P < 0.05$), rotating from a core-facing to a solvent-exposed orientation within the first nanosecond of simulation (*SI Appendix*, Fig. S6*C*).

To quantify the energetic consequences of these substitutions, we performed free-energy perturbation calculations to estimate the change in free energy of folding (ΔΔG) for each mutation in both the LAS and HAS conformations (Fig. 3*D*). L34K selectively destabilizes the HAS, where the side chain is buried, and has little effect on the LAS. By contrast, L34E destabilizes both conformations to a similar extent. WT^{LD} adopts HAS in the absence of the PD, implying that HAS is intrinsically lower in free energy than LAS. Equal destabilization of both states, as in L34E, will therefore not shift the equilibrium, whereas preferential destabilization of HAS by L34K favors adoption of the LAS. Thus, the calculations support the conclusion that substitution of a single toggle-switch residue can bias the LD toward LAS, but the outcome depends on how the specific side chain is accommodated within the protein core.

Toggle Switch Variant $L34K^{LD}$ Displays Rapid Mannose Association and Dissociation. NMR and mAb21 binding experiments establish that WT^{LD} and $L34K^{LD}$ adopt the same conformation upon mannose binding. To determine whether their binding kinetics are also comparable, we measured association and dissociation using biolayer interferometry (BLI), with biotinylated mannose immobilized on streptavidin sensors (Fig. 4 and *SI Appendix*, Fig. S7).

WT^{LD} and $L34K^{LD}$ exhibited strikingly different kinetic behaviors. WT^{LD} showed slow association and slow dissociation, whereas $L34K^{LD}$ displayed a rapid initial response followed by a slower phase during both association and dissociation (Fig. 4*A*), revealing substantial differences in their ligand-binding dynamics.

BLI data were collected at five concentrations of each LD variant (serial dilutions from 5 μM). Because none of several kinetic models (including a simple 1:1 binding model and a two-state binding model) adequately fit the multiphasic response curves, we used the empirical half-life ($t_{1/2}$), the time at which the measured response is 50% of the total response signal, to quantify binding behavior. During the association phase, $t_{1/2,\ assoc}$ reflects both on- and off-rates and is concentration dependent; during the dissociation phase $t_{1/2,\ dissoc}$ reports solely on ligand release and is therefore concentration-independent. Dissociation half-lives (averaged over all LD concentrations) are reported in Fig. 4*B* and association half-lives at 5 μM LD are in *SI Appendix*, Table S1.

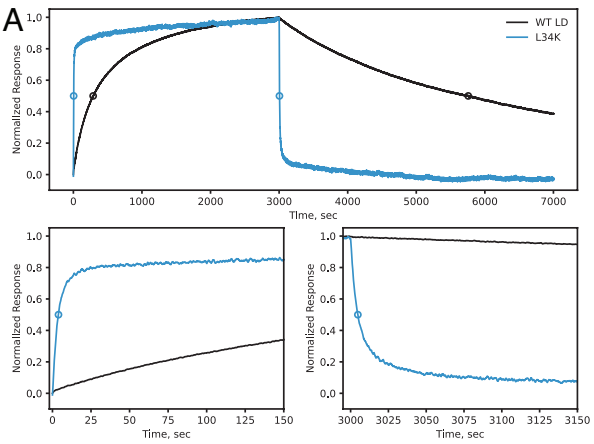

B

LD Variant	$t_{1/2,dissoc}$	Reference
WT^{LD}	2717 ± 45 sec	this work
$L34K^{LD}$	5.2 ± 0.6 sec	this work
WT^{LD}-WT^{PD}	2.7 sec	Kisiela et al., 2021
WT^{LD}-$FocH^{PD}$	2226 sec	Kisiela et al., 2021

Fig. 4. BLI response curves for WT^{LD} and $L34K^{LD}$ reveal differences in binding kinetics. Response curves at 5 μM LD are shown. Black, WT^{LD}; Blue, $L34K^{LD}$. The curves have been normalized to make comparison of the response rates easier to visualize. Non-normalized curves are presented in *SI Appendix*, Fig. S7. (*A*) *Top,* full BLI time courses with a 3,000 s association phase and a 4,000 s dissociation phase are shown. *Bottom,* zoomed views of the first 150 s of each phase. Circles indicate the $t_{1/2}$ values as given in (*B*) and *SI Appendix*, Table S1. (*B*) Comparison of dissociation half-times for isolated LDs (this work) and full-length FimH variants, as calculated from parameters reported in ref. 21. Specifically, $t_{1/2}$ is calculated as $Ln(2)/k_{off}$ for the *Bottom* two entries.

At the highest LD concentration tested, $L34K^{LD}$ reached 50% binding ~70-fold faster than WT^{LD} and achieved 50% dissociation over 500-fold faster than WT^{LD}. These results strongly suggest there is something inherently different between WT^{LD} and $L34K^{LD}$. In particular, while the NMR spectra are consistent with WT^{LD} and $L34K^{LD}$ adopting conformationally indistinguishable filled states, the term "HAS" explicitly associates that state with high affinity binding and is therefore not appropriate for the filled state of $L34K^{LD}$, which we refer to as "HAS-like."

Remarkably, the isolated LDs recapitulate the kinetic behavior of fimbrial $FimH^{FL}$ species, WT-FimH (WT^{LD}-WT^{PD}) and the chimeric form WT^{LD}- $FocH^{PD}$ (21). WT^{LD} and the (WT^{LD}-$FocH^{PD}$) both dissociate extremely slowly ($t_{1/2,dissoc}$ values > 30 min) and $L34K^{LD}$ and WT FimH (WT^{LD}-WT^{PD}) both dissociate rapidly ($t_{1/2,dissoc}$ of a few seconds) (Fig. 4*B*). Thus, a single toggle-residue substitution creates a single-domain lectin module that faithfully reproduces both the conformational and kinetic properties of a full-length adhesin.

The LD in HAS Undergoes Very Slow Conformational Dynamics. WT^{LD} and $L34K^{LD}$ dissociate from mannose at dramatically different rates despite adopting highly similar filled conformations by NMR, suggesting that the two variants differ in conformational dynamics. Prior NMR relaxation measurements (^{15}N T_1 and T_2) detected no unusual motions on the picosecond-to-nanosecond timescale (22) and our CPMG dispersion experiments revealed no millisecond-timescale dynamics (not shown). We therefore examined slower motions using hydrogen–deuterium exchange (HDX), which can report on rare backbone fluctuations occurring on timescales from minutes to hours (35). Ligand binding and conformational fluctuations can affect the solvent accessibility of backbone amides, influencing their deuterium uptake. Faster uptake (exchange) indicates greater solvent exposure, while more buried amide groups and those involved in hydrogen bonds display slower deuterium uptake.

We first used hydrogen-deuterium exchange by mass spectrometry (HDX–MS) to identify regions at peptide-level resolution that differ between WT^{LD} and $L34K^{LD}$. At exchange times ≥30 min, differences were observed between their filled states, indicating dynamic differences that occur on slow timescales (*SI Appendix*, Fig. S8). Peptides showing differential exchange clustered in the mannose-binding loops (residues 3 to 21, 42 to 55, and 130 to 151), but limited coverage across the LD sequence provided incomplete information that prevented more detailed analysis.

To obtain residue-level resolution, we performed NMR-monitored HDX. Lyophilized proteins were dissolved in D_2O, and ^1H–^{15}N HSQC spectra were collected every 5 min over 20 h. Exchange was quantified from the decay of resonance intensities (deuterium is silent in the NMR experiment), yielding residue-specific half-lives ($t_{1/2,\ H/D}$) (*SI Appendix*, Fig. S9 and Table S2). Residues fell into three classes: rapidly exchanging (<15 min; for example, blue trace for residue 27 Fig. 5*A*), intermediate (black traces for residue 11 and 27), or very slow (>20 h; for example blue and red traces for residue 11 Fig. 5*A*). A summary is provided in *SI Appendix*, Table S2; decay curves and exchange rates and $t_{1/2,\ H/D}$ are available as *SI Appendix*, Fig. S9.

We first compared apo-WT^{LD} and mannose-bound WT^{LD} to determine how ligand binding alters intradomain dynamics. Of 111 resonances analyzed, 30 exhibited ≥fivefold differences in exchange rates, with six differing by >100-fold (Fig. 5*B*). The largest slowing occurred in the mannose-binding loops and adjacent Clamp loop. Unexpectedly, a cluster of residues in the distal interdomain region also became more strongly protected upon mannose binding, despite showing no mannose-induced chemical shift changes (*SI Appendix*, Fig. S3). These amides are hydrogen bonded in the HAS structure, and their faster exchange in apo-WT^{LD} (i.e., empty-HAS) indicates that they undergo more frequent excursions into exchange-competent states. (These motions are still very infrequent, with $t_{1/2,\ H/D}$ values ranging from ~4 h to over 40 h.) Mannose binding therefore rigidifies not only the binding pocket but also the distal PD-interacting loops. This provides direct evidence for long-range allosteric coupling mediated by very slow backbone dynamics (Fig. 5 *B* and *C*).

We next compared filled WT^{LD} and $L34K^{LD}$. Despite their nearly identical NMR spectra, 32 residues exchange much faster in $L34K^{LD}$. Notably, residues in the mannose-binding loops are equally protected in both proteins, indicating that mannose affords similar protection in both species. However, Clamp-loop residues exchange 10 to 10^3-fold faster in $L34K^{LD}$, demonstrating that Clamp-loop dynamics are not determined solely by occupancy of the mannose-binding loops. The L34K mutation also accelerates exchange in the Swing loop (which contains residue 34), α-switch, Insertion loop, and Linker loop at the distal end of the LD (Figs. 1*A* and 5*C*). Importantly, the same regions that become

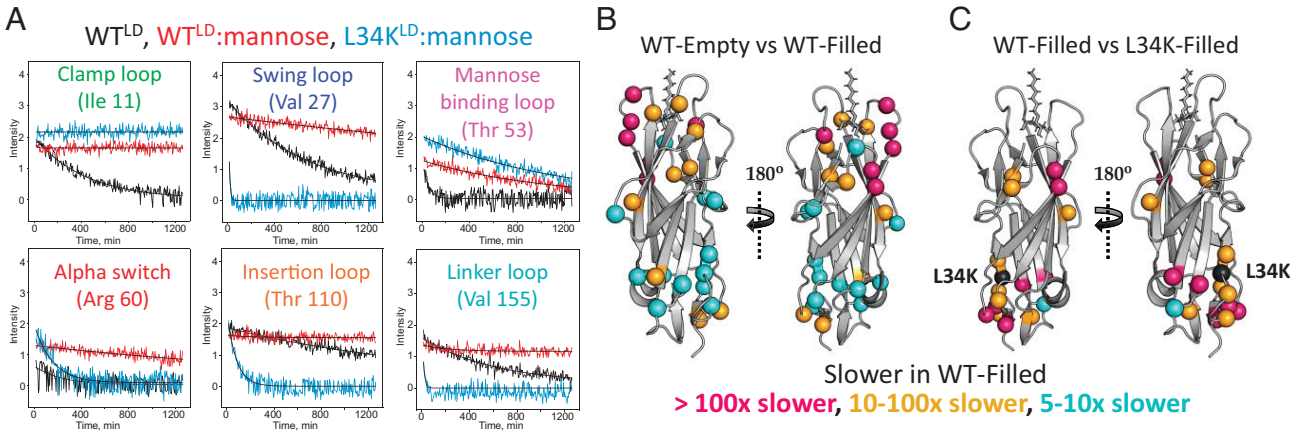

Fig. 5. HDX/NMR reveals different dynamics for filled WT^{LD} and $L34K^{LD}$ states. (*A*) Exemplary HDX traces for resonances that correspond to the indicated regions. WT empty-HAS in black; WT filled-HAS in red; L34K filled-HAS-like in blue. The y-axis is peak intensity; the x-axis is time. Traces that are flat and have intensity near/at zero are fully exchanged at the first time point; traces that are flat with intensity >0 have very slow deuterium exchange. (*B*) Residues whose exchange rates differ by fivefold or more between empty-HAS and filled-HAS in WT^{LD} are shown as spheres, with the image on the *Right* rotated 180° from the image on the *Left*. Pink, residues with rates that are >100-fold slower in filled-HAS; Orange, residues with rates that are between 10- and 100-fold slower in filled-HAS; Cyan, residues with rates that are between five- and 10-fold slower in filled-HAS (*C*) Same as Panel *B* but for residues whose exchange rates differ by fivefold or more between WT-filled HAS and L34K-filled HAS-like. The L34 side chain is shown in black spheres. The residues are listed in *SI Appendix*, Table S3.

protected upon mannose binding in WT^{LD} are destabilized in the filled HAS-like conformation by the L34K mutation, indicating that ligand binding and the toggle mutation act through a common allosteric network linking the interdomain region to the Clamp loop and binding pocket.

In conclusion, although allostery is often inferred from structural rearrangements, the HDX data reveal allosteric effects that are manifested as changes in dynamics within a single conformation. Similar phenomena have been reported for CAP–cAMP (36) and thrombin–thrombomodulin complexes (37). In FimH, these effects operate on much slower timescales, providing a mechanism by which very rare motions can govern ligand lifetime and, possibly, catch bond behavior.

FimH with the Toggle-Switch Mutant LD Forms Long-Lived Interactions Under Force. FimH forms catch bonds with mannose, meaning the average lifetime of the noncovalent interaction increases over a range of tensile force. Current models attribute this behavior to force-induced separation of the LD from the PD, relieving PD-mediated inhibition and allowing the LD to adopt a force-stabilized binding state (8, 16, 38). In this framework, WT^{LD} occupies LAS in the absence of force and mannose and transitions to a catch bond-competent state when force separates the LD from the PD. Because the L34K mutation stabilizes the LD in LAS even in the absence of the PD (Fig. 2), it provides a direct test of whether domain separation itself is required for catch bond formation. We addressed this question using two orthogonal force-dependent assays: atomic force microscopy (AFM) and red blood cell (RBC) binding under shear.

AFM reveals that L34K forms long-lived bonds under force. Three fimbrial constructs that adopt LAS in the absence of mannose were compared: WT^{LD}–WT^{PD}, $L34K^{LD}$–$FocH^{PD}$, and the disulfide-locked S-S^{LD}–$FocH^{PD}$. Because $FocH^{PD}$ lacks the interactions that stabilize the LD in LAS, these last two constructs are conformationally comparable to $L34K^{LD}$ and S-S^{LD}, but have a PD to integrate them into fimbriae for force spectroscopy. Fimbriae were immobilized and probed with a mannosylated-BSA–coated cantilever (Fig. 6*A*). Single-bond rupture events were detected in all three fimbrial samples but not in the no-fimbriae control (*SI Appendix*, Fig. S10 *A* and *B*). Force–extension profiles were comparable across constructs, allowing direct comparison.

The number of ruptures per pull did not differ significantly among the three variants, indicating that the number of activated bonds generated under force is similar. As the cantilever was retracted at constant velocity, a fimbria was stretched, leading first to its uncoiling at a constant force of 75 ± 15 pN for several seconds until the fimbria was fully uncoiled (*SI Appendix*, Fig. S10*B*). The rate at which fimbria broke during uncoiling provided a measurement of bond lifetime at constant force. After uncoiling, the fimbriae stretched elastically, causing force to increase at a rate of several thousand pN/s until the FimH–mannose interaction ruptured, providing a measure of the bond rupture force under a constant loading rate.

Rupture forces for each species are shown as violin plots in Fig. 6*B*. WT^{LD}-WT^{PD} exhibited the highest rupture force (~150 pN), $L34K^{LD}$-$FocH^{PD}$ ruptured at slightly lower forces (~120 pN), and S-S^{LD}-$FocH^{PD}$ ruptured only slightly above the fimbrial uncoiling force.

Bond lifetimes ($t_{1/2,dissoc,AFM}$) measured at 75 pN force further distinguished the species (Fig. 6*C*). The $t_{1/2,dissoc,AFM}$ for the WT^{LD}-WT^{PD} exhibited a half-life of 25 ± 8 s—nearly 10-times longer than that of the isolated WT^{LD}-WT^{PD} measured without force by BLI. $L34K^{LD}$-$FocH^{PD}$ also showed prolonged lifetimes under force (14.8 ± 1 s), approximately three-times longer than $L34K^{LD}$ measured by BLI without force (Fig. 4*B*). This increased lifetime under force is not consistent with slip bonds, which should decrease in lifetime nearly 100-fold at 80 pN (39). These data demonstrate that the L34K toggle-switch mutant forms long-lived force-stabilized associations, albeit with slightly weaker mechanical strength than WT.

L34K mediates shear-dependent bacterial adhesion to cells. FimH catch bond behavior can be detected as strong bacterial binding to RBCs that occurs under shear but not static conditions, reflecting force-dependent stabilization of FimH–mannose interactions (40, 41). Bacterial strains expressing WT^{LD} or $L34K^{LD}$ fused to either WT^{PD} or $FocH^{PD}$ were first confirmed to bind mannose-containing glycans under static conditions (*SI Appendix*, Fig. S11), ensuring that all strains displayed functional FimH. In static

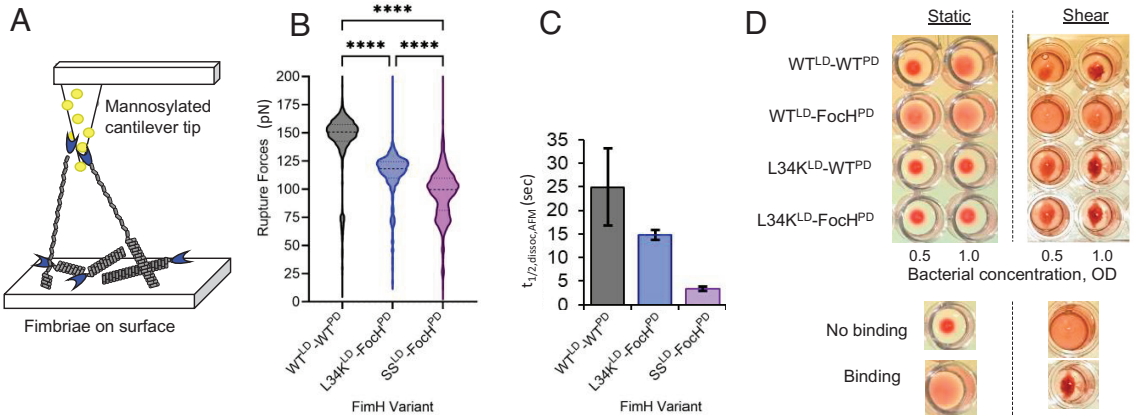

Fig. 6. Measurement of the mechanical properties of FimH variants. (*A*) Schematic of the experimental configuration, with fimbriae immobilized on the surface, and mannose-BSA immobilized on the cantilever tip. (*B*) Violin plot of rupture forces for the three FimH variants. A one-way ANOVA was used to determine statistical significance with Tukey's post hoc analysis of multiple comparisons. *** indicates $P < 0.0001$. (*C*) Estimate of the lifetime of the bonds at 75 pN from the fraction of bonds that break during uncoiling. (*D*) Bacterial binding and catch bond formation assayed by the RBC assay under static and dynamic conditions.

conditions, bacterial binding to RBCs is manifested by RBC agglutination visible as a diffuse pink "rosette" settled at the bottom of U-shaped wells. Rosette formation was clearly observed for WT^{LD}-$FocH^{PD}$ bacteria consistent with the ability of HAS to form strong interactions with mannose receptors in the absence of shear. Bacteria expressing WT^{LD}-$FimH^{PD}$ demonstrated a significantly weakened ability to form RBC rosettes, consistent with the WT^{LD} being mostly in LAS under static conditions. The inability to form RBC rosettes was even more obvious for bacteria expressing both L34K-containing FimH variants (Fig. 6*D*), indicating that the toggle mutant is consistently in its LAS conformation.

Strikingly different results were observed when samples were subjected to continuous shaking for 10 min immediately after mixing bacteria and RBCs (Fig. 6*D*). In contrast to the static case, both L34K-containing species induced RBC aggregation (observed as irregular, dense dark red patches in wells) as robustly and rapidly as WT^{LD}-WT^{PD}. As previously observed and discussed (21), WT^{PD}-$FocH^{PD}$—expressing bacteria were inferior in their ability to induce RBC aggregation under shear conditions, likely due to the very slow on-rate of FimH in HAS. Thus, consistent with the results from AFM, the toggle switch mutant effectively forms long-lived interactions with mannose under high shear-induced force conditions.

Together, the AFM, BLI, and RBC assays show that despite its rapid dissociation rate under static conditions, L34K forms long-lived force-stabilized interactions under mechanical force (AFM) and catch bonds as reflected in RBC aggregation under shear conditions (Fig. 6). Because L34K stabilizes the LD in LAS even in the absence of the PD, these results indicate that physical separation of the LD and PD may not be sufficient for catch bond formation. Instead, tensile force transmitted across the LD via the ligand-binding pocket could be required to drive the transition within the LD itself and produce force-dependent adhesion.

Discussion

Catch bonds are noncovalent interactions whose lifetimes increase under mechanical force like those induced by shear, in contrast to slip bonds that weaken under force (5, 8, 42, 43). In FimH, catch bond behavior enables bacterial adhesion to mannose moieties on host cell surfaces under urinary flow, promoting UTIs. Defining the molecular determinants that govern long-lived binding under force may therefore inform strategies to inhibit this ability.

The business end of FimH is its LD, which binds mannose through two binding loops, and is allosterically regulated by the PD, which anchors FimH to fimbriae. PD–LD interactions stabilize the LD in the LAS and disruption of this interface favors adoption of the HAS (16, 18). The LAS supports rapid association and dissociation, limiting prolonged interactions with free mannose, whereas the HAS associates more slowly but dissociates on timescales of minutes to hours once bound (5, 19, 21, 44). In the two-domain protein, the PD plays a central role in tuning these kinetics by enabling access to the LAS. Under force, the HAS can transition to an even longer-lived bound state characteristic of a catch bond, a process commonly attributed to force-induced separation of the PD and LD.

To identify the intrinsic determinants of LD binding kinetics, we sought a single-domain variant that spontaneously adopts the LAS and retains the ability to transition to HAS upon mannose binding. Among previously identified "toggle-switch" residues that differ between LAS and HAS conformations (21), we selected Leu34, a residue distant from the two known allosteric sites, namely the mannose-binding pocket and the PD interface. Substitution of Leu34 with charged residues revealed that L34K—but not L34E—induces spontaneous adoption of the LAS in the absence of the PD and mannose while allowing transition to HAS upon ligand binding. In the context of full-length FimH, mannose binding is no longer sufficient to overcome PD-mediated inhibition. Thus, a single amino acid substitution is sufficient to generate an LD that recapitulates the kinetic behavior underlying FimH function, validating strategies that stabilize the LAS as a potential route to inhibit FimH-mediated adhesion.

Previous studies have documented large differences in mannose dissociation rates among FimH variants, with a clear consensus that species that adopt the LAS in the absence of ligand dissociate ~10^3- to 10^5-fold faster than those that favor the HAS (5, 19, 21, 44). Consistent with this framework, the binding kinetics of isolated WT and L34K lectin domains reported here recapitulate both the association and dissociation behaviors of analogous full-length proteins (Fig. 4*B*), demonstrating that the kinetic determinants of FimH–mannose interactions are intrinsic to the LD. Differences in association rates can be rationalized by distinct starting conformations (LAS vs. HAS). In contrast, the >500-fold difference in dissociation rates cannot be explained by static structure, as both LDs adopt conformations that are essentially indistinguishable by NMR.

HDX measurements reveal that these dissociation rate differences are associated with distinct internal conformational dynamics. Backbone amide exchange reports on rare excursions from hydrogen-bonded conformations into solvent-accessible states, which we interpret as transient local "unsnapping" motions. Such events occur far less frequently in filled-WT^{LD} than in filled-$L34K^{LD}$ and localize primarily to the Clamp loop that forms one wall of the mannose-binding pocket and to the interdomain region at the opposite end of the LD. The Clamp loop adopts distinct open and closed conformations in the LAS and HAS, respectively (Fig. 1*B* and ref. 16). This loop is ~25 to 30 Å from the mutation site, so a 10^2- to 10^3-fold increase in Clamp-loop exchange in $L34K^{LD}$ indicates long-range coupling within the LD. We propose that burial of the charged Lys34 in HAS increases local dynamics in the interdomain region that are transmitted to the Clamp loop through a dynamically coupled network, representing a form of dynamic allostery (37) distinct from the canonical structural allostery imposed by the PD.

Despite its rapid dissociation under static conditions, L34K forms long-lived interactions under force, as measured by AFM and by RBC aggregation under shear conditions (Fig. 6). Without atomic-resolution structural information under force, the mechanism of catch bond formation remains speculative. One possibility is that force induces a distinct conformation accessible to both WT and L34K LDs. Alternatively, the catch bond state may closely resemble filled-HAS but exhibit further suppression of backbone dynamics, with Clamp-loop dynamics playing a central role in regulating dissociation. In HAS, the Clamp loop is supported by antiparallel β-strands hydrogen-bonded to neighboring strands, including the long β-strand that connects the binding pocket to the PD (*SI Appendix*, Fig. S12). Tensile force that pulls the PD away from a mannose-bound LD would act along this axis, effectively lengthening the LD and compressing local interatomic distances. In model systems, such compression strengthens hydrogen bonds (45); in the context of our unsnapping model, this would further reduce hydrogen-bond rupture, stabilizing the Clamp loop and extending bond lifetimes under force, i.e., forming catch bonds with ligands.

Emerging evidence suggests that systems known to form catch bonds also harbor intrinsic slow dynamics in the absence of force. HDX studies of von Willebrand factor and integrin α5β1 revealed backbone amide exchange on long timescales in both unbound and ligand-bound states (46–48), suggesting that slow dynamics may be a general, preexisting feature of force-responsive adhesion proteins (49). In this context, FimH exemplifies how modulation of long-timescale dynamics within a folded domain can tune ligand lifetimes under both static and mechanical conditions.

In summary, dissection of a single toggle residue in FimH reveals that force-dependent behaviors can be encoded within the intrinsic dynamics of a single domain, independent of large-scale domain rearrangements. One mutation is sufficient to rewire the energetic and dynamic landscape of the lectin domain, bypassing the pilin domain as an allosteric effector while preserving the defining ability of FimH to form long-lived bound states under force. These findings support a view in which catch bond formation arises not solely from force-induced structural transitions, but from modulation of preexisting, long-timescale dynamics that govern bond lifetimes. More broadly, this work highlights dynamic allostery as a general and tunable mechanism for mechanochemical regulation in adhesion proteins. By identifying specific structural elements whose dynamics dictate ligand lifetime, our results provide a conceptual framework for targeting force-stabilized conformational states, with implications for the design of anti-adhesive therapeutics and for understanding how mechanical forces shape molecular recognition in diverse contexts, both biological and nonbiological.

Materials and Methods

Generation of LD Variants by Site-Directed Mutagenesis. The *FimH* LD gene, cloned into the pET-22b plasmid, was subjected to site-directed mutagenesis using the QuickChange PCR-based method (50). Specifically designed primers were used to introduce the desired mutations. PCR amplification was performed with Phusion High-Fidelity DNA Polymerase under standard cycling parameters, followed by DpnI digestion to remove the original plasmid template. The resulting mutated plasmids were then transformed into *E. coli* Top10 cells, and colonies carrying the desired mutations were identified via sequencing. The verified plasmids were transformed into *E. coli* BL21(DE3) cells for protein expression.

Protein Expression and Purification.

Fimbriae. Bacteria expressing fimbriae were grown in 1 L cultures of LB broth supplemented with ampicillin and chloramphenicol, using 20 mL of an overnight starter culture for inoculation. Cultures were incubated at 37 °C while shaking at 125 rpm. Cells were harvested by centrifugation at 6,000 rpm for 15 min at 4 °C and resuspended in 50 mM Tris-HCl, 150 mM NaCl, pH 7.4 (buffer A). Cell lysis was performed using an Osterizer blender, with five cycles of 1-min blending followed by 1-min rest intervals on ice. Cell debris was removed by centrifugation at 12,000 rpm for 15 min at 4 °C. Fimbriae were purified by precipitation with 2 M $MgCl_2$ for 2 h at room temperature under continuous stirring. The precipitate, containing fimbriae, was collected by centrifugation at 15,000 rpm for 30 min at 4 °C and resuspended in buffer A. Fimbriae concentration was determined using the bicinchoninic acid (BCA) assay (51).

LDs. LD plasmids, containing a His-tag at their C terminus, were transformed into *E. coli* BL21 cells. Protein expression was induced with 0.5 mM IPTG overnight at 22 °C. For ^{15}N-labeling, cells were grown in minimal media with $^{15}NH_4Cl$. Cells were harvested, subjected to osmotic shock using Tris-HCl/sucrose buffers, followed by purification using nickel affinity and size-exclusion chromatography. Purified proteins were concentrated using a 10 kDa molecular weight cutoff (MWCO) centrifugal filter at 4,000 × *g*. Protein concentration was determined by measuring absorbance at 280 nm using a NanoDrop.

mAb21. mAb21 was generated from hybridoma cell cultures as previously described (29, 30) and purified using Protein G affinity chromatography. Briefly, supernatants containing secreted mAb21 were clarified by centrifugation at 10,000 × *g* for 20 min and filtered through a 0.22 μm membrane to remove cellular debris. The supernatant was loaded onto a Protein G column pre-equilibrated with binding buffer consisting of 20 mM sodium phosphate, pH 7.0 (buffer B) and the column was washed with 10 column volumes of the same buffer to remove unbound material. mAb21 was eluted with 100 mM glycine-HCl, pH 2.7, and eluted fractions were immediately neutralized with 1 M Tris-HCl, pH 9.0. The eluate was further purified by size-exclusion chromatography using a Superdex 200 column equilibrated with buffer B.

ELISA Experiments. To assess mAb21 binding, microtiter plate wells were coated with purified fimbriae at a concentration of 0.1 mg/mL in 0.02 M $NaHCO_3$ buffer pH 7.0 and incubated for 1 h at 37 °C in the absence or presence of mannose. After washing, mAb21 was added at a concentration of 0.5 μg/mL and incubated for 45 min. Bound antibodies were detected using a 1:5,000 dilution of HRP-conjugated goat anti-mouse Fc antibody. The reaction was developed at room temperature using 3,3′,5,5′-tetramethylbenzidine (TMB), and absorbance was measured at 650 nm.

MD Simulations.

General setup and simulations with single-point mutations. MD simulations were performed with variants of LD containing either the single-point mutation L34E or L34K, which were derived from WT^{LD} in HAS per analogy. The simulations were performed with the program NAMD (52) and the CHARMM22 force field (53) in explicit water. Details of the simulation setup can be found in *SI Appendix, Materials and Methods*. Two 50-ns long simulations were performed with each of the L34E and L34K variants. The simulations with the single-point mutations were compared with previously published runs performed with wild-type LD in HAS (33).

Free energy perturbation calculations to estimate the change in free energy of folding upon single-point mutations. To evaluate the change in free energy of folding due to single-point mutation in LD in both HAS and LAS, we made use of so called alchemical transformations (54), which were accomplished through free energy perturbation (FEP) calculations (55), similarly as in a previous study (56). Each alchemical transformation was performed in triplicate. The initial conformations for HAS were taken from snapshots along 50-ns long simulations performed in a previous study (56). To generate initial conformations for LAS, we performed two 50-ns long simulations starting with LD from the X-ray structure with PDB code 4XO9 (5) (only the first 160 N-terminal residues were kept). Details of the simulation setup can be found in Supplementary Materials and Methods.

NMR Data Acquisition, Processing, and Analysis. (^{1}H,^{15}N)-HSQC experiments were acquired on a Bruker Avance III 600 MHz spectrometer equipped with a cryoprobe. Samples were prepared in 20 mM Na_2HPO_4, 100 mM NaCl, and 0.5 μM EDTA at pH 6 (buffer D), with and without mannose. Backbone chemical shift assignments were obtained from standard triple-resonance experiments (HNCA and HNCACB) performed on a Bruker Avance III 800 MHz spectrometer equipped with a cryoprobe. All NMR experiments were conducted at 298 K. NMR data were processed using standard protocols in NMRPipe (57) and analyzed in NMRView (58).

For each sample, peaks in the (^{1}H,^{15}N)-HSQC spectra were picked using NMRViewJ at comparable levels. For spectra with known chemical shift assignments, the average amide CSP is calculated according to $\Delta\delta_{NH}$ (ppm) = sqrt [$\Delta\delta_H^2 + (\Delta\delta_N/5)^2$]. An assignment-free, pairwise spectral comparison is also possible. Considering each spectrum to contain peaks at coordinates (δ_H, δ_N/5), we calculate the matrix of all possible distances between peaks of one spectrum to the peaks in another spectrum. The pairwise similarity value – the chemical shift difference (CSD) score–is obtained from solving the two-dimensional rectangular assignment problem, wherein peaks are uniquely paired such that the sum of the distances between all peaks is minimized (59). We use the "linear_sum_assignment" function in the SciPy optimize module to compute these values, which are normalized by the number of pairs (60). In cases where samples have different numbers of peaks, for both the CSP and CSD scores, missing peaks are considered to have a distance of 0.5 ppm.

HDX-NMR sample preparation and data collection. To prepare samples for HDX-NMR, purified protein was first dialyzed extensively against Milli-Q water and subsequently lyophilized. The resulting powder was reconstituted in a deuterium oxide (D_2O)-based buffer containing 20 mM Na_2HPO_4, 100 mM NaCl, and 0.5 μM EDTA, adjusted to pD 5.6. NMR data acquisition was initiated 10 min after dissolution. A series of two-dimensional [^{1}H,^{15}N]-HSQC spectra were then recorded at 5-min intervals over a 20-h period to monitor D_2O uptake.

BLI Data Acquisition, Processing, and Analysis. BLI streptavidin biosensors were hydrated in PBS buffer pH 7.2, containing 2% (w/v) BSA and 0.2% Tween-20 (buffer E). The proteins were also in the same buffer. Biotinylated mannose (0.05 ug/mL) was immobilized to the sensors for 600 s and then washed with buffer E for another 600 s. The sensors were then dipped in a serial dilution of five protein concentrations (5 to 0.312 μM) for 3,000 s during the association phase. The dissociation phase was carried out by moving the sensors into buffer E for 4,000 s. Data were collected on an Octet R8 instrument (Sartorius).

High-quality response curves were obtained for all five serial dilutions. The data were not sufficiently well-fit by several different models including a simple 1:1 binding model and a two-state binding model. We instead quantified ligand binding kinetics of the 5 μM traces using a model free empirical metric, the half-lives ($t_{1/2,on}$ and $t_{1/2,off}$), where $t_{1/2}$ is the time at which the measured response is 50% of the total signal starting from either the beginning of the association or dissociation timepoints, respectively.

HDX-MS Data Acquisition, Processing, and Analysis. FimH LD proteins were exposed to an 85% D_2O buffer (Buffer D), with and without mannose at room temperature for varying durations–4 s, 1 min, 30 min, and 20 h–to monitor hydrogen–deuterium exchange over time. To prepare fully deuterated controls, proteins were incubated in the same buffer at 75 °C for 30 min. The exchange reaction was halted by adding a chilled quenching solution (1.6% formic acid), followed by immediate flash freezing in liquid nitrogen. Frozen samples were later thawed and subjected to enzymatic digestion using immobilized NEP-2. The resulting peptides were analyzed with a Waters Synapt G2-Si mass spectrometer configured using a custom LEAP PAL automation system (61). Peptide identification was carried out through tandem MS on a Thermo Orbitrap Fusion Tribrid or via MSE on the Synapt G2-Si. Data were processed using either ProteinProspector (UCSF) or ProteinLynx Global SERVER (Waters). Deuterium incorporation levels were calculated with HDExaminer 3.0 (Sierra Analytics), and data analyses were performed using pyHXExpress (62).

AFM Data Acquisition, Processing, and Analysis. Type 1 pili expressing either WT^{LD}-WT^{PD}, $L34K^{LD}$-$FocH^{PD}$, and $S\text{-}S^{LD}$-$FocH^{PD}$ were immobilized at a concentration of 10 to 20 μg/mL in 0.02 M $NaHCO_3$ buffer on 35 mm tissue culture dishes (Corning) for 75 min at 37 °C. Dishes were then washed three times with 0.2% bovine serum albumin in phosphate-buffered saline (PBS-BSA) and stored overnight at 4 °C in the same buffer to block nonspecific binding. For the negative control, the pili immobilization step was omitted. Olympus Biolever cantilevers were functionalized by incubation with 200 μg/mL mannosylated BSA (man-BSA) for 75 min at 37 °C, followed by washing and overnight storage in 0.2% BSA-PBS at 4 °C. Force measurements were conducted using an Asylum MFP-3D Atomic Force Microscope. Cantilevers (spring constants of 4.38 and 6.36 pN/nm) were brought into contact with the sample surface to allow bonds to form between FimH and mannose, then retracted at a constant speed of 2 μm/s while collecting data at 2,400 Hz. Pulling experiments were performed in 0.2% BSA-PBS. Approximately 100 force curves (pulls) were collected at each of three to five different positions per condition on each of 3 d. Although multiple bonds often formed during each approach, the uncoiling of pili during retraction and the wide distribution of pili lengths of *E. coli* resulted in highly variable fimbrial extension lengths, and therefore well-separated rupture events, allowing clear resolution of individual bond rupture forces, as illustrated in *SI Appendix*, Fig. S10. This ensures that less than 1% of rupture force measurements reflect more than one bond, as explained in the calculations in the supplemental methods. Bond rupture forces were calculated using a custom automated script in Matlab. Rupture force was defined as the difference between the force immediately before rupture and the average postrupture baseline, where that difference is greater than four SD in the force measurements in a region of constant force. To reduce the chance the two events were counted as a single event, it was also required that the force dropped in every time step during the rupture. Most nonspecific binding in the negative control occurred within 0.25 μM of the surface, so this was set as a minimum distance threshold to identify specific bonds.

Bacterial Adhesion Assay. Bacteria were cultured overnight at 37 °C under static conditions. The following day, cultures were pelleted by centrifugation, washed twice with PBS, and resuspended to an optical density of 2.0 at 540 nm (OD_{540}). Flat-bottom 96-well plates were coated with 100 μL of bovine RNase B (20 μg/mL) in 0.02 M sodium bicarbonate buffer and incubated at 37 °C for 1 h. Wells were subsequently blocked with 0.2% BSA in PBS at 37 °C for 30 min and then aspirated. Control wells were coated with 0.2% BSA in PBS alone. Bacterial suspensions were added to the coated wells and incubated for 45 min at 37 °C. Wells were then extensively washed with PBS to remove nonadherent bacteria, dried at 60 °C for 10 min, and stained with 0.1% crystal violet (Becton Dickinson) for 20 min at room temperature. After washing with water, 50% ethanol was added to solubilize the stain, and absorbance was measured at 600 nm.

RBC Agglutination Assay. To assess the effect of fluidic shear on *E. coli* adhesion, we performed RBC agglutination assays under both static and dynamic conditions using guinea pig RBCs (Colorado Serum Company, Inc., Denver, CO). For static conditions, a standard RBC rosette assay was conducted. Serial dilutions of *E. coli* suspensions (starting at OD_{540} = 2.0) were prepared in PBS. A total of 50 μL of each bacterial dilution was mixed with 50 μL of a 1% RBC suspension in a U-bottom 96-well microtiter plate precoated with BSA to prevent nonspecific binding. Plates were incubated at room temperature without agitation for 60 min, after which images were taken. For dynamic conditions, a modified rocking assay was used. Equal volumes (50 μL each) of *E. coli* suspension (OD_{540} = 2.0) and 1% RBC suspension were combined on a BSA-coated concave serological glass plate. The plate was continuously rocked at room temperature to simulate shear forces, and images were taken after 20 min to assess RBC agglutination.

Data, Materials, and Software Availability. The data and Jupyter Notebooks for the CSD and BLI analyses are available at https://doi.org/10.5281/zenodo.18715524 (63). All other data are included in the manuscript and/or *SI Appendix*.

ACKNOWLEDGMENTS. We thank Angelo Ramos for assistance with protein production, Natalie Stone for support with the collection and processing of hydrogen-deuterium exchange by mass spectrometry (HDX-MS) data, Anna Manchenko for assistance with red blood cell data collection, and Dagmara Kisiela for support with the mAb21 binding experiments. Biolayer interferometrydata were collected at the Hans Neurath Biophysical Core at the University of Washington. HDX-MS data were acquired at the University of Washington's Proteomics Resource (UWPR95794). Computational simulations were performed on the Expanse supercomputer at the San Diego Supercomputing Center through an ACCESS allocation (Grant No. TG-BIO240027), supported by the NSF. Thanks go to Peter Brzovic, Nicole Raniszewski, and Ronald Stenkamp for valuable discussions and critical reading. This work was supported by NIH Grants K99GM141364 (to P.M.), F31HL147462 (to M.Y.M.), R01AI171570 (to R.E.K. and E.V.S.), R01HL153253 (to G.I.), and R01AI119675 (to E.V.S. and W.E.T.).

Author affiliations: [a]Department of Biochemistry, University of Washington, Seattle, WA 98195; [b]Department of Bioengineering, University of Washington, Seattle, WA 98195; and [c]Department of Microbiology, University of Washington, Seattle, WA 98195

Author contributions: P.M., W.E.T., E.V.S., and R.E.K. designed research; P.M., G.I., L.A.C., M.Y.M., and E.V.S. performed research; L.M.T. contributed new reagents/analytic tools; P.M., L.M.T., G.I., L.A.C., M.Y.M., M.K.J., W.E.T., E.V.S., and R.E.K. analyzed data; and P.M. and R.E.K. wrote the paper.

1. R. D. Klein, S. J. Hultgren, Urinary tract infections: Microbial pathogenesis, host–pathogen interactions and new treatment strategies. *Nat. Rev. Microbiol.* **18**, 211–226 (2020).
2. A. Sheikh *et al.*, Highly conserved type 1 pili promote enterotoxigenic *E. coli* pathogen-host interactions. *PLoS Negl. Trop. Dis.* **11**, e0005586 (2017).
3. V. Kalas *et al.*, Evolutionary fine-tuning of conformational ensembles in FimH during host–pathogen interactions. *Sci. Adv.* **3**, e1601944 (2017).
4. D. J. Schwartz *et al.*, Positively selected FimH residues enhance virulence during urinary tract infection by altering FimH conformation. *Proc. Natl. Acad. Sci. U.S.A.* **110**, 15530–15537 (2013).
5. M. M. Sauer *et al.*, Catch-bond mechanism of the bacterial adhesin FimH. *Nat. Commun.* **7**, 10738 (2016).
6. W. E. Thomas *et al.*, Recombinant FimH adhesin demonstrates how the allosteric catch bond mechanism can support fast and strong bacterial attachment in the absence of shear. *J. Mol. Biol.* **434**, 167681 (2022).
7. W. Thomas, Catch bonds in adhesion. *Annu. Rev. Biomed. Eng.* **10**, 39–57 (2008).
8. W. Thomas *et al.*, Catch-bond model derived from allostery explains force-activated bacterial adhesion. *Biophys. J.* **90**, 753–764 (2006).
9. L. M. Nilsson, W. E. Thomas, E. V. Sokurenko, V. Vogel, Elevated shear stress protects *Escherichia coli* cells adhering to surfaces via catch bonds from detachment by soluble inhibitors. *Appl. Environ. Microbiol.* **72**, 3005–3010 (2006).
10. W. E. Thomas, V. Vogel, E. Sokurenko, Biophysics of catch bonds. *Annu. Rev. Biophys.* **37**, 399–416 (2008).
11. M. A. Schembri, K. Kjaergaard, E. V. Sokurenko, P. Klemm, Molecular characterization of the *Escherichia coli* FimH adhesin. *J. Infect. Dis.* **183**, S28–S31 (2001).
12. N. Foroogh, M. Rezvan, K. Ahmad, S. Mahmood, Structural and functional characterization of the FimH adhesin of uropathogenic *Escherichia coli* and its novel applications. *Microb. Pathog.* **161**, 105288 (2021).
13. K. A. Krogfelt, H. Bergmans, P. Klemm, Direct evidence that the FimH protein is the mannose-specific adhesin of *Escherichia coli* type 1 fimbriae. *Infect. Immun.* **58**, 1995–1998 (1990).
14. F. Lupo, M. A. Ingersoll, M. A. Pineda, The glycobiology of uropathogenic *E. coli* infection: The sweet and bitter role of sugars in urinary tract immunity. *Immunology* **164**, 3–14 (2021).
15. J. Bouckaert *et al.*, Receptor binding studies disclose a novel class of high-affinity inhibitors of the *Escherichia coli* FimH adhesin. *Mol. Microbiol.* **55**, 441–455 (2005).
16. I. Le Trong *et al.*, Structural basis for mechanical force regulation of the adhesin FimH via finger trap–like β sheet twisting. *Cell* **141**, 645–655 (2010).
17. V. B. Rodriguez *et al.*, Allosteric coupling in the bacterial adhesive protein FimH*. *J. Biol. Chem.* **288**, 24128–24139 (2013).
18. P. Aprikian *et al.*, Interdomain interaction in the FimH adhesin of *Escherichia coli* regulates the affinity to mannose*. *J. Biol. Chem.* **282**, 23437–23446 (2007).
19. S. Rabbani *et al.*, Conformational switch of the bacterial adhesin FimH in the absence of the regulatory domain: Engineering a minimalistic allosteric system. *J. Biol. Chem.* **293**, 1835–1849 (2018).
20. D. I. Kisiela *et al.*, Conformational inactivation induces immunogenicity of the receptor-binding pocket of a bacterial adhesin. *Proc. Natl. Acad. Sci. U.S.A.* **110**, 19089–19094 (2013).
21. D. I. Kisiela *et al.*, Toggle switch residues control allosteric transitions in bacterial adhesins by participating in a concerted repacking of the protein core. *PLoS Pathog.* **17**, e1009440 (2021).
22. S. Vanwetswinkel *et al.*, Study of the structural and dynamic effects in the FimH Adhesin upon α-d-Heptyl Mannose binding. *J. Med. Chem.* **57**, 1416–1427 (2014).
23. J. Liu, L. A. N. Amaral, S. Keten, Conformational stability of the bacterial adhesin, FimH, with an inactivating mutation. *Proteins* **89**, 276–288 (2021).
24. P. Magala, R. E. Klevit, W. E. Thomas, E. V. Sokurenko, R. E. Stenkamp, RMSD analysis of structures of the bacterial protein FimH identifies five conformations of its lectin domain. *Proteins* **88**, 593–603 (2020).
25. L. E. Kay, M. Ikura, R. Tschudin, A. Bax, Three-dimensional triple-resonance NMR spectroscopy of isotopically enriched proteins. *J. Magn. Reson.* **1969**, 496–514 (1990).
26. B. Fiege *et al.*, The tyrosine gate of the bacterial lectin FimH: A conformational analysis by NMR spectroscopy and X-ray crystallography. *ChemBioChem* **16**, 1235–1246 (2015).
27. E. V. Sokurenko, V. Tchesnokova, G. Interlandi, R. Klevit, W. E. Thomas, Neutralizing antibodies against allosteric proteins: Insights from a bacterial adhesin. *J. Mol. Biol.* **434**, 167717 (2022).
28. D. I. Kisiela *et al.*, Inhibition and reversal of microbial attachment by an antibody with parasteric activity against the FimH adhesin of uropathogenic *E. coli*. *PLoS Pathog.* **11**, e1004857 (2015).
29. V. Tchesnokova *et al.*, Type 1 Fimbrial Adhesin FimH elicits an immune response that enhances cell adhesion of *Escherichia coli*. *Infect. Immun.* **79**, 3895–3904 (2011).
30. V. Tchesnokova *et al.*, Integrin-like allosteric properties of the catch bond-forming FimH adhesin of *Escherichia coli**. *J. Biol. Chem.* **283**, 7823–7833 (2008).
31. K. L. Hvorecny *et al.*, Antibodies disrupt bacterial adhesion by ligand mimicry and allosteric interference. *Nat. Commun.* **16**, 10590 (2025).
32. E. V. Sokurenko *et al.*, Valency conversion in the type 1 fimbrial adhesin of *Escherichia coli*. *Mol. Microbiol.* **41**, 675–686 (2001).
33. G. Interlandi, W. E. Thomas, Mechanism of allosteric propagation across a β-sheet structure investigated by molecular dynamics simulations. *Proteins* **84**, 990–1008 (2016).
34. S. Miller, J. Janin, A. M. Lesk, C. Chothia, Interior and surface of monomeric proteins. *J. Mol. Biol.* **196**, 641–656 (1987).
35. G. R. Masson *et al.*, Recommendations for performing, interpreting and reporting hydrogen deuterium exchange mass spectrometry (HDX-MS) experiments. *Nat. Methods* **16**, 595–602 (2019).
36. N. Popovych, S.-R. Tzeng, M. Tonelli, R. H. Ebright, C. G. Kalodimos, Structural basis for cAMP-mediated allosteric control of the catabolite activator protein. *Proc. Natl. Acad. Sci. U.S.A.* **106**, 6927–6932 (2009).
37. R. B. Peacock, E. A. Komives, Hydrogen/Deuterium exchange and nuclear magnetic resonance spectroscopy reveal dynamic allostery on multiple time scales in the serine protease thrombin. *Biochemistry* **60**, 3441–3448 (2021).
38. O. Yakovenko *et al.*, FimH forms catch bonds that are enhanced by mechanical force due to allosteric regulation*. *J. Biol. Chem.* **283**, 11596–11605 (2008).
39. L. A. Carlucci, K. C. Johnson, W. E. Thomas, FimH-mannose noncovalent bonds survive minutes to hours under force. *Biophys. J.* **123**, 3038–3050 (2024).
40. W. E. Thomas, E. Trintchina, M. Forero, V. Vogel, E. V. Sokurenko, Bacterial adhesion to target cells enhanced by shear force. *Cell* **109**, 913–923 (2002).
41. S. Szunerits *et al.*, Differentiation of Crohn's disease-associated isolates from other pathogenic *Escherichia coli* by fimbrial adhesion under shear force. *Biology* **5**, 14 (2016).
42. E. V. Sokurenko, V. Vogel, W. E. Thomas, Catch-bond mechanism of force-enhanced adhesion: Counterintuitive, elusive, but … widespread? *Cell Host Microbe* **4**, 314–323 (2008).
43. M. Mathelié-Guinlet, F. Viela, D. Alsteens, Y. F. Dufrêne, Stress-induced catch-bonds to enhance bacterial adhesion. *Trends Microbiol.* **29**, 286–288 (2021).
44. O. Yakovenko, V. Tchesnokova, E. V. Sokurenko, W. E. Thomas, Inactive conformation enhances binding function in physiological conditions. *Proc. Natl. Acad. Sci. U.S.A.* **112**, 9884–9889 (2015).
45. S. Fanetti, M. Citroni, K. Dziubek, M. M. Nobrega, R. Bini, The role of H-bond in the high-pressure chemistry of model molecules. *J. Phys. Condens. Matter* **30**, 094001 (2018).
46. M. A. Blenner, X. Dong, T. A. Springer, Structural basis of regulation of von Willebrand Factor binding to Glycoprotein Ib*. *J. Biol. Chem.* **289**, 5565–5579 (2014).
47. K. Bonazza *et al.*, Von Willebrand factor A1 domain stability and affinity for GPIbα are differentially regulated by its O-glycosylated N- and C-linker. *eLife* **11**, e75760 (2022).
48. Y. Su, R. E. Iacob, J. Li, J. R. Engen, T. A. Springer, Dynamics of integrin α5β1, fibronectin, and their complex reveal sites of interaction and conformational change. *J. Biol. Chem.* **298**, 102323 (2022).
49. A. V. Belyaev, I. V. Fedotova, Molecular mechanisms of catch bonds and their implications for platelet hemostasis. *Biophys. Rev.* **15**, 1233–1256 (2023).
50. H. Liu, J. H. Naismith, An efficient one-step site-directed deletion, insertion, single and multiple-site plasmid mutagenesis protocol. *BMC Biotechnol.* **8**, 91 (2008).
51. P. K. Smith *et al.*, Measurement of protein using bicinchoninic acid. *Anal. Biochem.* **150**, 76–85 (1985).
52. L. Kalé *et al.*, NAMD2: Greater scalability for parallel molecular dynamics. *J. Comput. Phys.* **151**, 283–312 (1999).
53. A. D. MacKerell Jr. *et al.*, All-atom empirical potential for molecular modeling and dynamics studies of proteins. *J. Phys. Chem. B* **102**, 3586–3616 (1998).
54. C. Chipot, D. A. Pearlman, Free energy calculations, the long and winding gilded road. *Mol. Simul.* **28**, 1–12 (2002).
55. R. W. Zwanzig, High-temperature equation of state by a perturbation method. II. Polar gases. *J. Chem. Phys.* **23**, 1915–1922 (1955).
56. G. Interlandi, Destabilization of the von Willebrand factor A2 domain under oxidizing conditions investigated by molecular dynamics simulations. *PLoS ONE* **13**, e0203675 (2018).
57. F. Delaglio *et al.*, NMRPipe: A multidimensional spectral processing system based on UNIX pipes. *J. Biomol. NMR* **6**, 277–293 (1995).
58. B. A. Johnson, "Using NMRView to visualize and analyze the NMR spectra of macromolecules" in *Protein NMR Techniques*, A. K. Downing, Ed. (Humana Press, 2004), pp. 313–352.
59. D. F. Crouse, On implementing 2D rectangular assignment algorithms. *IEEE Trans. Aerosp. Electron. Syst.* **52**, 1679–1696 (2016).
60. P. Virtanen *et al.*, SciPy 1.0: Fundamental algorithms for scientific computing in Python. *Nat. Methods* **17**, 261–272 (2020).
61. M. J. Watson *et al.*, Simple platform for automating decoupled LC–MS analysis of hydrogen/deuterium exchange samples. *J. Am. Soc. Mass Spectrom.* **32**, 597–600 (2021).
62. L. M. Tuttle, R. E. Klevit, M. Guttman, A framework for automated multimodal HDX-MS analysis. bioRxiv [Preprint] (2025). https://doi.org/10.1101/2025.03.13.643099 (Accessed 5 February 2025).
63. P. Magala, L. M. Tuttle, R. E. Klevit. FimH_L34K_analysis. Zenodo. https://doi.org/10.5281/zenodo.18715524. Deposited 20 February 2026.